

Large-eddy simulation of the diurnal cycle of shallow cumulus convection over land

By A. R. BROWN^{1*}, R. T. CEDERWALL², A. CHLOND³, P. G. DUYNKERKE⁴, J.-C. GOLAZ⁵,
M. KHAIROUTDINOV⁵, D. C. LEWELLEN⁶, A. P. LOCK¹, M. K. MACVEAN¹, C.-H. MOENG⁷,
R. A. J. NEGGERS⁸, A. P. SIEBESMA⁸ and B. STEVENS⁹

¹*Met Office, UK*

²*Lawrence Livermore National Laboratory, USA*

³*Max-Planck-Institut für Meteorologie, Germany*

⁴*Utrecht University, The Netherlands*

⁵*Colorado State University, USA*

⁶*West Virginia University, USA*

⁷*National Center for Atmospheric Research, USA*

⁸*Royal Netherlands Meteorological Institute, The Netherlands*

⁹*University of California Los Angeles, USA*

(Received 23 July 2001; revised 7 December 2001)

SUMMARY

Large-eddy simulations of the development of shallow cumulus convection over land are presented. Many characteristics of the cumulus layer previously found in simulations of quasi-steady convection over the sea are found to be reproduced in this more strongly forced, unsteady case. Furthermore, the results are shown to be encouragingly robust, with similar results obtained with eight independent models, and also across a range of numerical resolutions. The datasets produced are already being used in the development and evaluation of parametrizations used in numerical weather-prediction and climate models.

KEYWORDS: ARM GCSS Intercomparison

1. INTRODUCTION

The representation of shallow cumulus convection is an important issue for numerical weather-prediction and climate models (e.g. Tiedtke *et al.* 1988), and in recent years a number of studies have addressed the problems of trying to increase our understanding of the process and of improving the parametrizations used. In many cases (as described later) these studies have used large-eddy simulation (LES) models, as these can provide many detailed diagnostics which would be difficult or impossible to obtain directly from experimental data. It is also possible to test sensitivity to different parameters individually. Of course, there is a continuing need to evaluate the reliability of the model results using such observations as are available and also by examining the level of sensitivity to model formulation and resolution. A number of intercomparison projects, performed as part of the Global Energy and Water Cycle Experiment Cloud System Study (GCSS) programme (Browning 1993), have proved valuable in this respect.

Much of the recent work has focused on a case designed by Siebesma and Cuijpers (1995) based on the Barbados Oceanographic and Meteorological Experiment (BOMEX). For this trade-wind case they found results consistent with the available observations but inconsistent with the assumptions made in parametrization schemes. In particular, their fractional entrainment rates into the cumulus ensemble were an order of magnitude larger than those used in the parametrizations, and their detrainment rates were larger than the entrainment rates (indicating a convective mass flux which decreased with height). Support for the reliability of the results of these simulations came

* Corresponding author: Met Office, London Road, Bracknell RG12 2SZ, UK.

e-mail: andy.brown@metoffice.com

© Royal Meteorological Society, 2002. A. R. Brown's, A. P. Lock's and M. K. MacVean's contributions are Crown copyright.

from an intercomparison study (Pier Siebesma, personal communication) which showed generally good agreement between a large number of independent models for a variety of statistics, and also from the finding that these results were insensitive to a five-fold increase in resolution (Brown 1999a). Improved performance was obtained from a one-dimensional model when its parametrizations were modified to use entrainment and detrainment rates consistent with those from the LES (Siebesma and Holtslag 1996).

Other cases have also been studied. For example Stevens *et al.* (2001) performed another intercomparison based on observations from the Atlantic Trade Wind Experiment (ATEX). The results for most of the cumulus layer were reasonably consistent with those from the BOMEX case, although there were differences (and a greater spread in model results) close to the inversion due to the higher relative humidities in ATEX leading to a tendency to form stratiform cloud which was not present in the BOMEX simulations. Grant and Brown (1999) also performed 'modified' BOMEX cases which, in conjunction with the standard case, they used to propose simple scalings for some properties of the cumulus layer.

One feature common to all of the above studies is that they have considered relatively statistically steady convection over the sea. Comparatively little attention has been paid to cases of shallow cumulus convection over land, which will typically have forcing that is both stronger and time varying. Potentially the unsteadiness of the problem might make such cases more difficult for the large-eddy models. There is also an interest in whether results such as scalings for cumulus layer, developed based solely on the over-sea cases, are general enough to still be applicable. In the longer term, an increased understanding of the processes controlling the development of shallow cumulus may also be of help in understanding that of deep convection, the initial development of which will typically be poorly resolved in cloud-resolving models which have to use much larger domains.

This paper seeks to start to address some of these issues by presenting results from a large-eddy model study of the development of shallow cumulus convection over land. The case presented forms the sixth intercomparison of GCSS Working Group 1, and is also being used as part of the European Cloud Systems project. It is based on an idealization of observations made at the Southern Great Plains (SGP) site of the Atmospheric Radiation Measurement (ARM) Program on 21 June 1997. The site consists of *in situ* and remote-sensing instrumented clusters arrayed across approximately 140 000 km² in Oklahoma and Kansas. On the day in question, cumulus clouds developed at the top of an initially clear convective boundary layer. The main foci will be on assessing the reliability of the model results (through intercomparison, extra numerical sensitivity tests and the use of observational results where available) and on comparing the results with those previously obtained in the studies of shallow cumulus over the sea.

2. CASE DESCRIPTION

(a) *Initial conditions*

Figure 1 shows the ARM SGP central-facility sonde profiles of potential temperature θ and total-water mixing ratio r_T at 1130 UTC (0530 local time), 1430, 1730 and 2030 UTC on 21 June 1997.

At 1130 UTC, there was a shallow stable boundary layer, but the inversion soon disappeared once the surface heat flux became positive (at around 1230 UTC) and, as expected, the boundary layer tended to warm and deepen through the day. Profiles obtained with a variational assimilation method (Zhang and Lin 1997; Zhang *et al.*

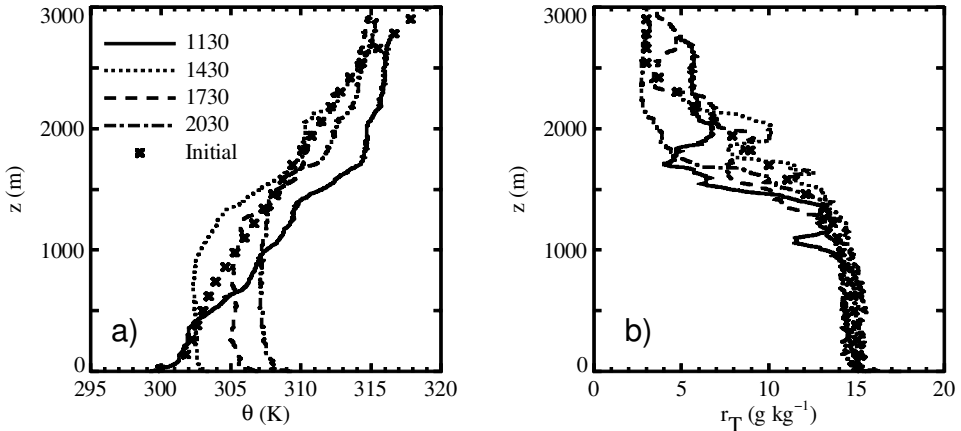


Figure 1. Central-facility sonde profiles of (a) potential temperature and (b) total-water mixing ratio. The times in the key are UTC. The crosses indicate the initial profiles used in the simulations.

2001) based on observations from over the entire SGP site (an area of approximately 365×300 km) showed a similar development, but were not used in the construction of initial profiles because of a loss of structure in the vertical.

Given that the resolution used, in order to allow the use of a domain large enough to reasonably represent shallow cumulus convection, would inevitably be far too coarse to explicitly resolve turbulence in the stable boundary layer, there seemed to be little point in commencing the simulations much before sunrise. Accordingly, it was decided to start at 1130 UTC. The initial profiles used are shown as crosses in Fig. 1 (and also tabulated in the appendix for any readers who may wish to repeat these simulations). Note that the initial potential-temperature profile is not closely matched to the profile observed at that time. The reason for this is that the central-facility observations show a significant cooling from 500 to 2000 m between 1130 and 1430 UTC which is not provided by the diagnosed large-scale forcings (possibly because the forcings are designed to represent averages over the entire SGP site rather than local forcings at a single site). For this reason it seemed sensible to start with a cooler profile than that given by the observations. On the other hand, it was not desirable to start with a profile exactly like that observed at 1430 UTC, as budget considerations suggested that the models could not then warm sufficiently to agree with the observations at later times. The chosen profile was therefore a compromise between the sonde profiles from 1130 and 1430 UTC. Another minor modification that was made was to slightly increase the potential-temperature gradient above 2500 m. This was done in order to ensure that the clouds did not reach too close to the models' tops. However, it should be stressed that the cloud tops in the simulations only reached 2500 m relatively late in the day, and tests without this modification (using a deeper than standard domain) confirmed that its effect was not particularly significant.

The central-facility sondes indicated that the wind direction was almost constant (in height and time) and Fig. 2 shows the observed profiles of wind speed. At the time when the case was set up, detailed estimates of the time and height variation of the geostrophic wind, and of any large-scale advective tendencies of the wind components, were not available. Accordingly there seemed to be little chance of matching the detailed behaviour (e.g. the deceleration in the lowest kilometre between 1130 and 1430 UTC, and the subsequent acceleration to give the 1730 UTC profile). Instead, for simplicity,

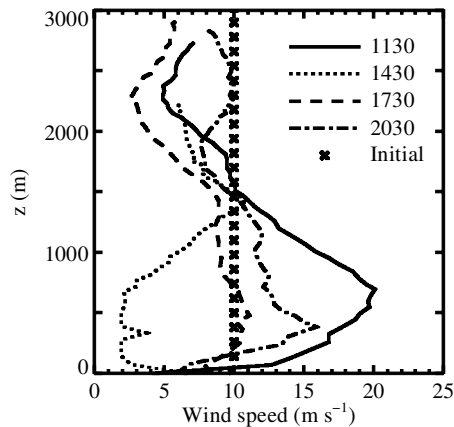


Figure 2. Central-facility sonde profiles of wind speed. The times in the key are UTC. The crosses indicate the initial profile used in the simulations.

the initial horizontal wind (u, v) was set to $(10, 0) \text{ m s}^{-1}$ at all levels. As buoyancy production of turbulence dominated over shear production throughout most of the day, the details of the modelled wind fields seem unlikely to have had a significant impact on the cloud fields and scalar transport (Brown 1999b).

Turbulence was initiated by imposing random temperature perturbations at each grid point in the lowest 200 m (maximum amplitude at any model level decreasing linearly from 0.1 K at the surface to zero at 200 m). Models which carry a prognostic equation for subgrid turbulence kinetic energy (TKE) set the initial subgrid TKE to $0.15(1.0 - z/150) \text{ kg m}^{-1}\text{s}^{-2}$ for height $z < 150 \text{ m}$, and to zero for $z \geq 150 \text{ m}$. The surface pressure was set to 97 000 Pa.

(b) Surface boundary condition

Figure 3 shows the surface sensible- and latent-heat fluxes measured at the SGP central facility. The strong diurnal cycle is clear, and the maximum values are far in excess of those used in simulations of the BOMEX and ATEX over-sea cases (e.g. compare with the 9 W m^{-2} sensible-heat and 150 W m^{-2} latent-heat fluxes used for BOMEX). Note also the significant change in Bowen ratio, with a typical value of around 0.3 here, compared to 0.06 for BOMEX. A simple piecewise-linear representation of the time variation of the surface scalar fluxes was constructed (shown in Fig. 3 and given in the appendix), and these fluxes were then imposed in the model simulations.

The surface roughness length was set to 0.035 m (a characteristic value for the ARM site). Monin–Obukhov similarity was then used to get the friction velocity (u_*) at each surface point from the velocity at each point of the lowest interior model level.

(c) Large-scale forcing and radiation

For completeness, details of the representation of the effects of large-scale advection and radiation are given in the appendix. However, it should be noted that the forcings are weak compared to that from the surface, and tests showed that complete removal of these terms had only a minor impact on the simulations.

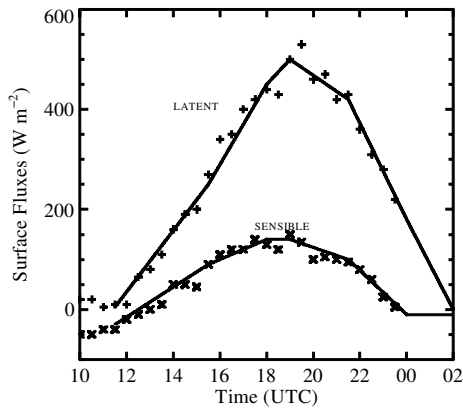


Figure 3. Observed surface sensible-heat and latent-heat fluxes at the central facility (symbols) and the values imposed in the models (solid lines).

TABLE 1. SUMMARY OF PARTICIPATING MODELS

Model	Participating scientists	Formulation	Subgrid model	Scalar advection
Met Office	Brown, Lock, Macvean	Anelastic	Smagorinsky	Monotone
NCAR	Moeng	Boussinesq	TKE	Monotone
WVU	Lewellen	Boussinesq	TKE	Monotone
MPI	Chlond	Boussinesq	TKE	Monotone
KNMI	Neggers, Siebesma	Boussinesq	TKE	Centred
CSU-LEM/UOK	Khairoutdinov	Anelastic	TKE	Monotone
CSU-RAMS	Golaz	Compressible	TKE	Centred
UCLA	Stevens	Anelastic	Smagorinsky	Monotone

Model sources are the National Center for Atmospheric Research (NCAR), West Virginia University (WVU), Max Planck Institute (MPI), Koninklijk Nederlands Meteorologisch Instituut (KNMI), Colorado State University Large Eddy Model as developed with the University of Oklahoma (CSU-LEM/UOK), the CSU Regional Atmospheric Modelling System (CSU-RAMS), and the University of California, Los Angeles (UCLA).

A large-scale horizontal pressure gradient was applied, equivalent, with a Coriolis parameter of $8.5 \times 10^{-5} \text{ s}^{-1}$ (as appropriate for a latitude of 36°N), to a geostrophic wind of $(10, 0) \text{ m s}^{-1}$.

(d) Participating models and numerical set-up

Eight independent LES models were used to run the case, and a brief summary of some aspects of the standard configurations of these models is given in Table 1. Four models used the Boussinesq approximation, while three used the anelastic approximation, and one was fully compressible. Six used a subgrid model that carried TKE as a prognostic variable, while two used a version of the Smagorinsky model. For scalar advection, six used some form of monotone scheme, while two used a centred scheme. Even within these broad headings there was considerable further variability in the details of the implementation, for example in the specification of the length-scale in the subgrid models. Microphysics parametrizations were switched off for the standard intercomparison run, and all models used all-or-nothing saturation schemes except for the MPI and WVU models which included subgrid partial-cloudiness schemes.

The domain size used was $6400 \times 6400 \text{ m}$ in the horizontal, with a depth of 4400 m . The vertical grid spacing was 40 m , and the horizontal spacing used was 66.7 m , except

in the MPI model in which it was 100 m. To prevent gravity-wave reflection from their upper lids, most models used damping layers above 3500 m.

The simulations were run from 1130 UTC 21 June until 0200 UTC 22 June. Statistics were averaged over each full hour of the simulation. These included mean, flux and variance profiles averaged over the entire horizontal domain. In this paper $\langle \phi \rangle$ is used to indicate such an average of a quantity ϕ , with the quoted time being the mid-point of the averaging period; primes denote perturbations from these averages. Additionally, conditionally sampled diagnostics were calculated, averaging over all cloudy points and also over all core points (where cores are defined to be cloudy points that are positively buoyant relative to the layer mean). Accordingly the total amount of data collected is far in excess of that which could possibly be presented in this paper. Any reader who would find the full datasets useful (e.g. in connection with work evaluating the performance of single-column models) is encouraged to contact the authors from whom they are available.

In spite of the differences in the models detailed above, it has not proved possible to attribute such differences as do exist between their results to any particular aspects of their formulations (e.g. the results from models with TKE subgrid models do not appear to differ systematically from those with Smagorinsky models). This is consistent with past experience (e.g. Stevens *et al.* 2001). Furthermore, as will be shown in the next section, the differences between the results of the different models tend to be fairly small (and certainly too small for us to be able to say which is 'best' on the basis of the observations). For these reasons, the plots in the next section will show each simulation result in the same way, with no attempt to identify which is which, and the interpretation will then be mainly in terms of a typical LES result. In a few places, where there is a significant spread in the results, some of the outlying results will be identified in the text.

3. RESULTS

The results will be presented as follows. First the general development of the simulations is discussed, concentrating on the evolution of the mean profiles and on the growth and decay of the cumulus clouds. Next consideration is given to the turbulence structure of the convective boundary layer (before cloud formation) and of the subcloud layer (after cloud formation). Some characteristics of the cloud layer are then discussed, concentrating in particular on similarities and differences from those observed in the earlier studies of convection over the sea. Finally some sensitivity studies are discussed, examining both numerical and physical issues.

(a) General development

In order to give a general overview of the development of the eight simulations, Fig. 4 shows the evolution of the mean profiles of potential temperature and total-water mixing ratio, while Fig. 5 shows time series of total cloud fraction (which is the fraction of the vertical columns which contain cloud), maximum cloud fraction at any one level, cloud-base height and cloud-top height. The evolution of the profiles is broadly as expected, with the depth of mixing increasing through the day. The first clouds form at around 1500 UTC. After this time the cloud base rises slowly through the day (from around 700 m at 1500 UTC to 1200 m at 2400 UTC). This increase of cloud-base height with time is consistent with the warming of the subcloud-layer air shown in Fig. 4. However, it contrasts with the almost constant cloud-base heights found in each of the BOMEX and ATEX cases, and a closure assumption for a convection

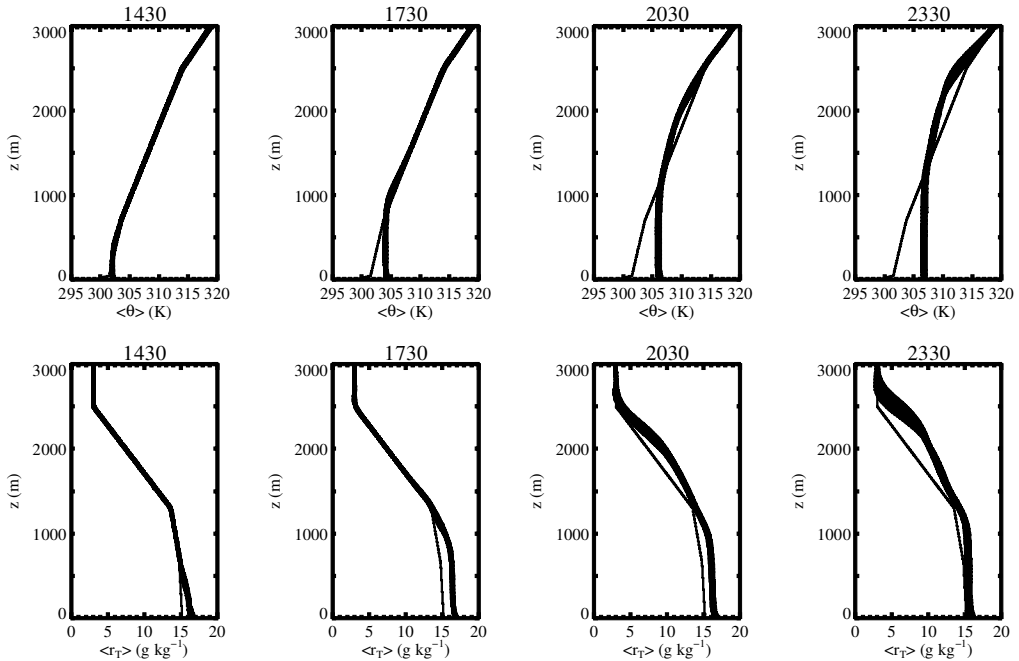


Figure 4. Profiles of potential temperature (θ) and total-water mixing ratio (r_T) at various times UTC from the eight different models. In almost all panels the lines from the different models are sufficiently close together that they overlap, and so we actually see the range of LES results rather than individual solutions. The light lines in each panel show the initial profiles.

parametrization based on constancy of cloud-base height (Stevens *et al.* 2001) would not be applicable here. Cloud-top growth is steady, but fairly slow, with the cloud-top heights only reaching their maximum values (of between 2500 and 3000 m) at around 2100 UTC, about six hours after initial cloud formation. The largest cloud fractions occur early within the growth period at around 1700 UTC and, at just under 30% total cover, are considerably larger than obtained for BOMEX (which gave 10 to 15% cover). After 1700 UTC the cloud fractions slowly decline (to around 15% total cover at 2200 UTC) before falling away more quickly as the surface forcing dies away.

In view of initial concerns that this unsteady situation might prove to be a difficult case for the LES models, the degree of consistency in their solutions is most encouraging. Indeed, the spread in the results (both in statistics presented thus far and more generally) appears to be no greater than previously obtained in the BOMEX intercomparison (Pier Siebesma, personal communication). The most significant differences are probably in the distance penetrated into the capping inversion (e.g. see the r_T profiles at 2330 UTC), an area in which the results of different simulations of the BOMEX case also tend to show increased variability (e.g. Brown 1999a).

The compromises which had to be made in the construction of the initial profiles, and uncertainties in the estimates of the large-scale forcings, make it difficult to make meaningful quantitative comparisons with the observations. One encouraging feature is that both the micro-pulse lidar and the Belfort ceilometer at the central facility support the LES result of cloud fractions tending, after the initial increase, to decrease with time (Fig. 5(a)). However, the increase in cloud cover occurs more slowly in the simulations, and we cannot say whether this is indicative of problems with the models, or is simply

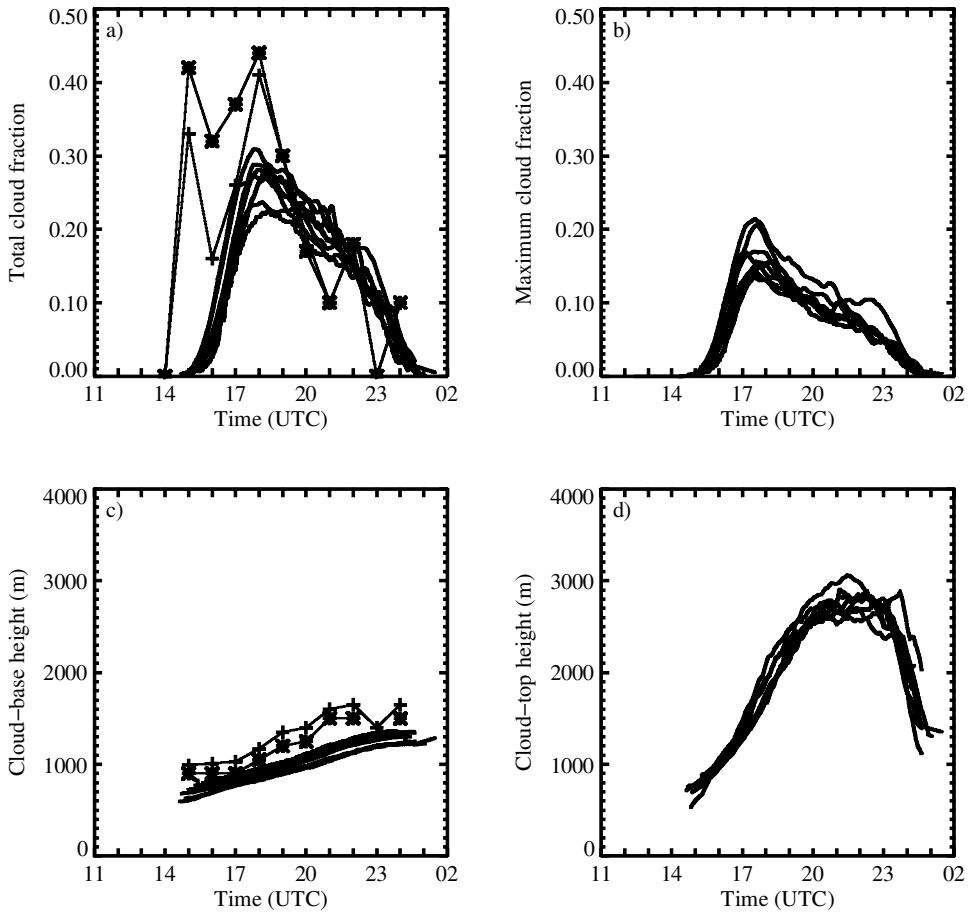


Figure 5. Time series (smoothed over one hour) from the eight simulations. (a) Total cloud fraction, (b) maximum cloud fraction at any one level, (c) cloud-base height and (d) cloud-top height. In (a) and (c) the stars are the observations of the micro-pulse lidar, while the crosses are the observations of the Belfort Ceilometer at the central facility.

the result of an unfair comparison. One plausible explanation is that, given their initial profiles and forcings, the models could not possibly achieve the 1430 UTC $\langle\theta\rangle$ profile shown in Fig. 1, and that the deeper observed mixed layer would favour earlier cloud formation. A sensitivity test with the Met Office model, in which the initial $\langle\theta\rangle$ profile below 1 km was made more unstable in order to more closely match the 1430 UTC profile, lent support to this idea, as this run attained its maximum cloud cover (of around 0.4) about two hours earlier than the standard run with the same model (although, as noted in section 2(a), it could not then warm up sufficiently to match the observed profiles at later times). Another area of discrepancy between the standard runs and the observations is in the prediction of cloud-base height. While the modelled rates of rise of cloud base are similar to those of the observed at the central facility, the LES cloud bases are consistently lower (Fig. 5(c)). This is consistent with the models showing total-water mixing ratios of around 16 g kg^{-1} in the mixed layer for much of the day, while the observed values are around 15 g kg^{-1} . Once again though, it proved possible to largely remove this discrepancy in a sensitivity test by making an arbitrary, but still

plausible, change to the initial profiles. In this case this involved modifying the $\langle r_T \rangle$ profile below 2 km to be consistent with the driest of the sonde observations shown in Fig. 1 (cf. the standard profile which is close to the wettest). Entrainment of drier air into the subcloud layer then led to reduced $\langle r_T \rangle$ values there, and resulted in the cloud base being over 200 m higher for most of the run.

(b) *Convective boundary-layer and subcloud-layer turbulence*

Convective boundary-layer turbulence has been extensively studied, both experimentally and through modelling. Hence the results of the present simulations can be checked for consistency with relatively well-established results. This is particularly useful, as the lack of comparable data for the cloud layer will prevent detailed evaluation of the results in this region.

Figure 6 shows profiles of the total vertical and horizontal velocity variances at 1430 and 2030 UTC. The 1430 UTC results are discussed first. At this time, before the formation of the first clouds, the simulated boundary layers have a depth (based on the height of the minima in the buoyancy flux profiles) $z_i \simeq 450$ m. Given the imposed surface buoyancy fluxes, this leads to w_* (convective velocity-scale) values of around unity, while u_* is around 0.6 m s^{-1} . This implies values of $-z_i/L$ (where L is the Obukhov length) of around 2. Observations (e.g. Nicholls and Readings 1979; Grant 1986) suggest that only moderate levels of instability are required in order for the vertical velocity variance to scale convectively, and it is therefore reassuring to find good agreement between the model results and the best fit to the free convective data of Lenschow *et al.* (1980). In contrast, $-z_i/L \simeq 2$ is insufficiently unstable for the influence of shear not to have a significant impact on the horizontal velocity variances (Nicholls and Readings 1979). Modelled values of around $0.7w_*^2$ in mid-boundary layer are in fact quite consistent with those obtained in earlier boundary-layer LES studies at comparable stabilities (Mason 1992; Moeng and Sullivan 1994), although there is a considerable amount of scatter amongst the individual results. The existence of maxima in the $\langle u'u' \rangle$ profiles towards the top of the boundary layer (present in all simulations except that with the CSU-LEM/UOK model, and most pronounced in that with the WVU model) is consistent with convective updraughts spreading horizontally as they approach the inversion. Past experience (Paul Mason, personal communication) has indicated that the magnitude of the variance in this region may be sensitive to the details of the subgrid model.

At 2030 UTC clouds are present in all of the simulations. However, observations from the GARP* Atlantic Tropical Experiment (Nicholls and LeMone 1980) suggest that standard boundary-layer scaling should still be applicable in the subcloud layer. Taking z_i to be equal to the height of the buoyancy flux minimum which occurs close to cloud base, we have $z_i \simeq 1100$ m, $w_* \simeq 1.7 \text{ m s}^{-1}$, $u_* \simeq 0.6 \text{ m s}^{-1}$ and $-z_i/L \simeq 9$. This is sufficiently convective for both the vertical and horizontal velocity variances to be expected to scale convectively. From Fig. 6 it can be seen that the model results for $\langle w'w' \rangle$ in the subcloud layer are indeed in good agreement with those predicted using the best fit to the data of Lenschow *et al.* (1980). Higher up, the secondary maxima in the $\langle w'w' \rangle$ profiles are associated with the cumulus activity. For the horizontal velocity variance, nominally free-convective observations typically show values in the middle of the atmospheric boundary layer of around $0.4w_*^2$. The present modelled values are rather smaller, at around $0.25w_*^2$ in the middle of the subcloud layer. However, they are consistent with those typically obtained in LES of the dry free-convective boundary

* Global Atmospheric Research Program.

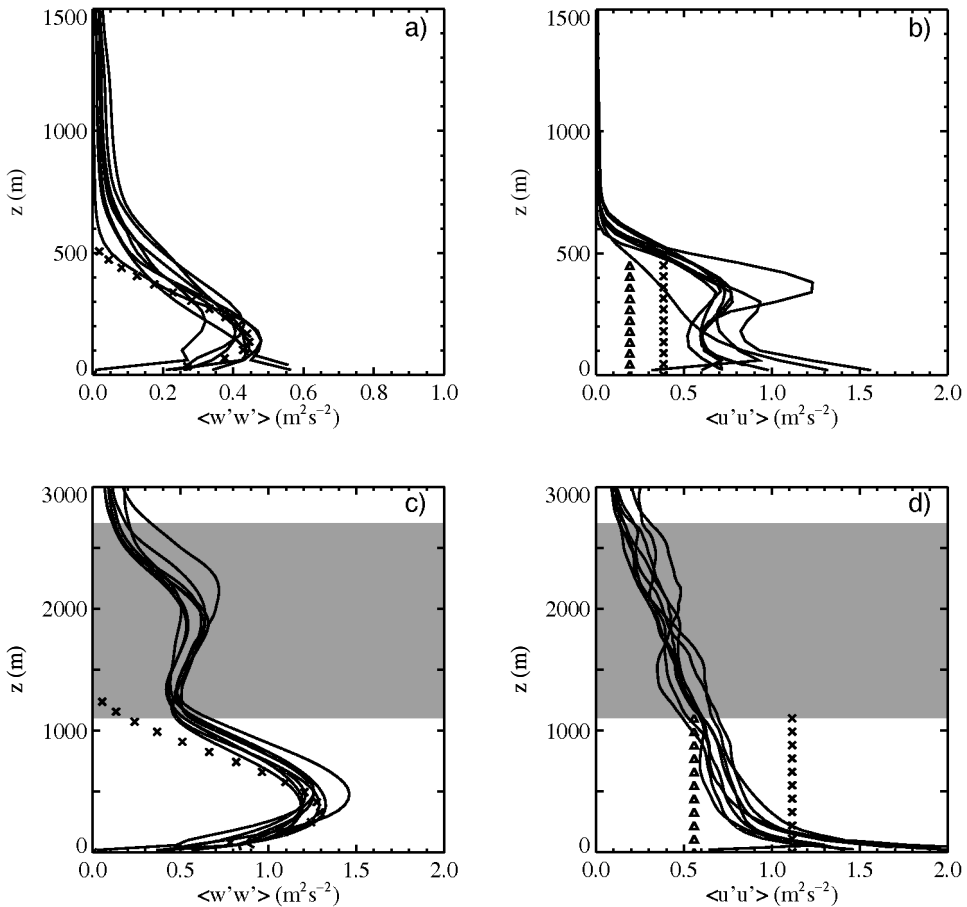


Figure 6. Profiles of $\langle w'w' \rangle$ and $\langle u'u' \rangle$, the vertical and horizontal velocity variances (including subgrid contributions) from the eight simulations at (a)–(b) 1430, and (c)–(d) 2030 UTC. The crosses in (a) and (c) show the function $\langle w'w' \rangle = 1.8(z/z_i)^{2/3}(1 - 0.8z/z_i)^2 w_*^2$ (Lenschow *et al.* 1980). Here z_i is the depth and w_* is the velocity-scale of the convective boundary layer at 1430 UTC and of the subcloud layer at 2030 UTC (see text). The crosses in (b) and (d) show $\langle u'u' \rangle = 0.4w_*^2$, while the triangles show $\langle u'u' \rangle = 0.2w_*^2$. The shaded regions in (c) and (d) indicate the cloud layer at this time (defined as being between the mean cloud-base and cloud-top heights from the eight simulations).

layer (e.g. Nieuwstadt *et al.* 1991; Moeng and Sullivan 1994). The reason for the discrepancy between LES and observed values of $\langle u'u' \rangle$ has long been debated (it could indicate a problem with the LES, or it could be the result of an unfair comparison due to the observations being influenced by larger-scale forcing or wind shear). The main point here is that, as the scaled subcloud-layer horizontal variances remain consistent with those obtained in dry boundary-layer studies, the present results are still consistent with the idea that the turbulence structure of the subcloud layer is largely unaffected by the presence of cumulus aloft. Interestingly though, the $\langle u'u' \rangle$ profiles do not show maxima towards the top of the subcloud layer corresponding to those seen towards the top of the boundary layer at 1430 UTC. Presumably this is because some of the convective updraughts continue through the lifting condensation level to form cumulus clouds, and so there is less horizontal spreading than occurs in the absence of clouds.

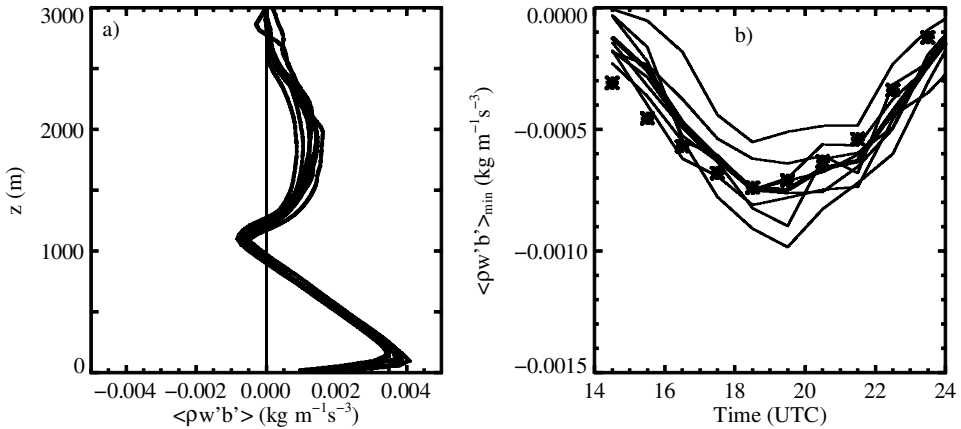


Figure 7. (a) Profiles of resolved buoyancy flux $\langle \rho w' b' \rangle$ at 2030 UTC. (b) Time series of the minimum value of buoyancy flux ($\langle \rho w' b' \rangle_{\min}$). The light lines show the results from the individual simulations, while the heavy line shows the average of these results. The stars show -0.13 times the imposed surface buoyancy flux.

As discussed in Nicholls and LeMone (1980), the insensitivity of the scaled variances to the presence of the cumulus clouds is associated with the similarity of the buoyancy flux profiles (and hence buoyancy production of TKE) in cases with and without clouds. As an example, Fig. 7(a) shows the simulated resolved buoyancy flux $\langle \rho w' b' \rangle$ profiles at 2030 UTC, where ρ is density. The profiles in the subcloud layer are strongly reminiscent of those obtained in clear convective boundary layers, with a linear decrease through most of the layer and values at the top which are of order -0.15 times the surface buoyancy flux. Indeed, assuming that the minimum value of the buoyancy flux (which occurs at the top of the clear boundary layer or subcloud layer) should remain a fixed fraction of the surface flux has been suggested as a plausible closure assumption for use in a parametrization scheme. This case provides a good opportunity to test this, as it has a strongly time-varying surface flux. Figure 7(b) shows time series from the eight simulations of the minimum value of the resolved flux. The mean of the simulation results (shown bold) remains close to -0.13 times the imposed surface flux (shown as stars) over most of the diurnal cycle. Furthermore, if estimates of the subgrid fluxes (not shown) are added to the resolved fluxes, then this improves the agreement before about 1600 UTC without having a significant impact at later times. The results from the individual simulations do show considerable scatter (although not beyond that typically found in comparisons of modelled entrainment fluxes at the top of clear convective boundary layers, e.g. Nieuwstadt *et al.* (1991)). Nevertheless they are each individually broadly consistent with the idea of the cloud-base buoyancy flux being a fixed fraction of the surface flux, with only the value of that fraction varying somewhat from model to model. For reference it is noted that the smallest resolved entrainment fluxes are consistently given by the CSU-RAMS model, with the Met Office model next, while the MPI model gives the largest fluxes. However, as noted in section 2(d), it has not proved possible to explain these differences in terms of differences in the model formulations.

(c) Cloud layer

Direct validation of the details of the simulated cloud layers is difficult, and the main interest in this section will be in comparing the present results with those previously

obtained in studies of cumulus over the sea. In order to do this, Fig. 8 shows profiles of core fraction, core mass flux and core fractional entrainment rate (calculated as in Siebesma and Cuijpers 1995) at 1830 and 2030 UTC. The earlier time was chosen as one at which the cloud layer is deepening relatively rapidly, while the latter is representative of the results obtained once the clouds are close to their full depth. Also shown for comparison in the right column are the BOMEX results (simulation HR-CONV) of Brown (1999a). The results of this simulation lie very close to those of others of this case (e.g. Siebesma and Cuijpers 1995) and may therefore be considered to show a typical LES result for BOMEX.

As originally found by Siebesma and Cuijpers (1995), the BOMEX simulation gives core fraction and mass flux peaking just above cloud base, and then monotonically decreasing with height. The ARM case has considerably higher cloud base and top, but it is immediately apparent that these results concerning the profile shapes carry over to this over-land case, both in the rapidly growing stage (1830 UTC) and in the more steady period (2030 UTC). The diagnosed fractional entrainment rates are also of the same order of magnitude as those from BOMEX. Other statistics (e.g. conditionally sampled over all cloudy points rather than just the cores) and visualizations of the cloud fields also support the idea that the cloud layer in this case is not fundamentally different from that in the BOMEX case. At any given time the clouds all tend to have the same base, but varying tops, with many shallow clouds and relatively few deep ones. The finding that the time and area-averaged cloud cover decreases with height is a result of this distribution of cloud tops (and does not reflect the characteristics of individual clouds). In the present case the cloud base rises through the day. At the same time the depth of the deepest clouds gradually increases, although the majority of the clouds remain significantly shallower.

In spite of the broad similarities with the BOMEX case noted above, the details of some of the profile shapes do appear to change over time. As shown in Fig. 8, the mass flux at 2030 UTC decreases only relatively slowly from around 1300 m (where the maximum value occurs) up to 1800 m before falling off more quickly. The BOMEX profile shows a similar structure (with the vertical gradient of the mass flux changing noticeably in this case at around 1400 m). The fractional entrainment rates are also fairly independent of height in the middle sections of the cloud layers from both the ARM simulation at 2030 UTC and from the BOMEX simulation. In contrast, the 1830 UTC mass flux and fractional entrainment-rate profiles from the ARM case show a rather different structure, with a much more uniform decrease through the entire depth of the cloud layer. This suggests that the non-equilibrium nature of the cloud layer at this time does have some influence. We will return to this issue in section 4.

The typical values of the mass flux and fractional entrainment rates in the present case are also rather different from those in the BOMEX and ATEX simulations. For example, Fig. 8 shows a maximum mass flux value at 2030 UTC of around $0.065 \text{ kg m}^{-2} \text{ s}^{-1}$. This is considerably larger than the BOMEX (and ATEX) values of around $0.025 \text{ kg m}^{-2} \text{ s}^{-1}$. Note, however, that here the subcloud-layer velocity-scale w_* has a value of 1.7 m s^{-1} , compared to around 0.7 m s^{-1} for BOMEX and ATEX. Grant (2001) proposed that the maximum value of the mass flux should be proportional to ρw_* , and normalizing the maximum value by ρw_* does indeed lead to a value of around 0.035 for all three cases. Thus the increase in mass flux appears to be largely explained by the stronger forcing in the present over-land case. However, the present results do indicate that it would be over-simplistic to suggest that the mass flux is controlled solely by w_* —the modelled maximum mass fluxes decrease monotonically

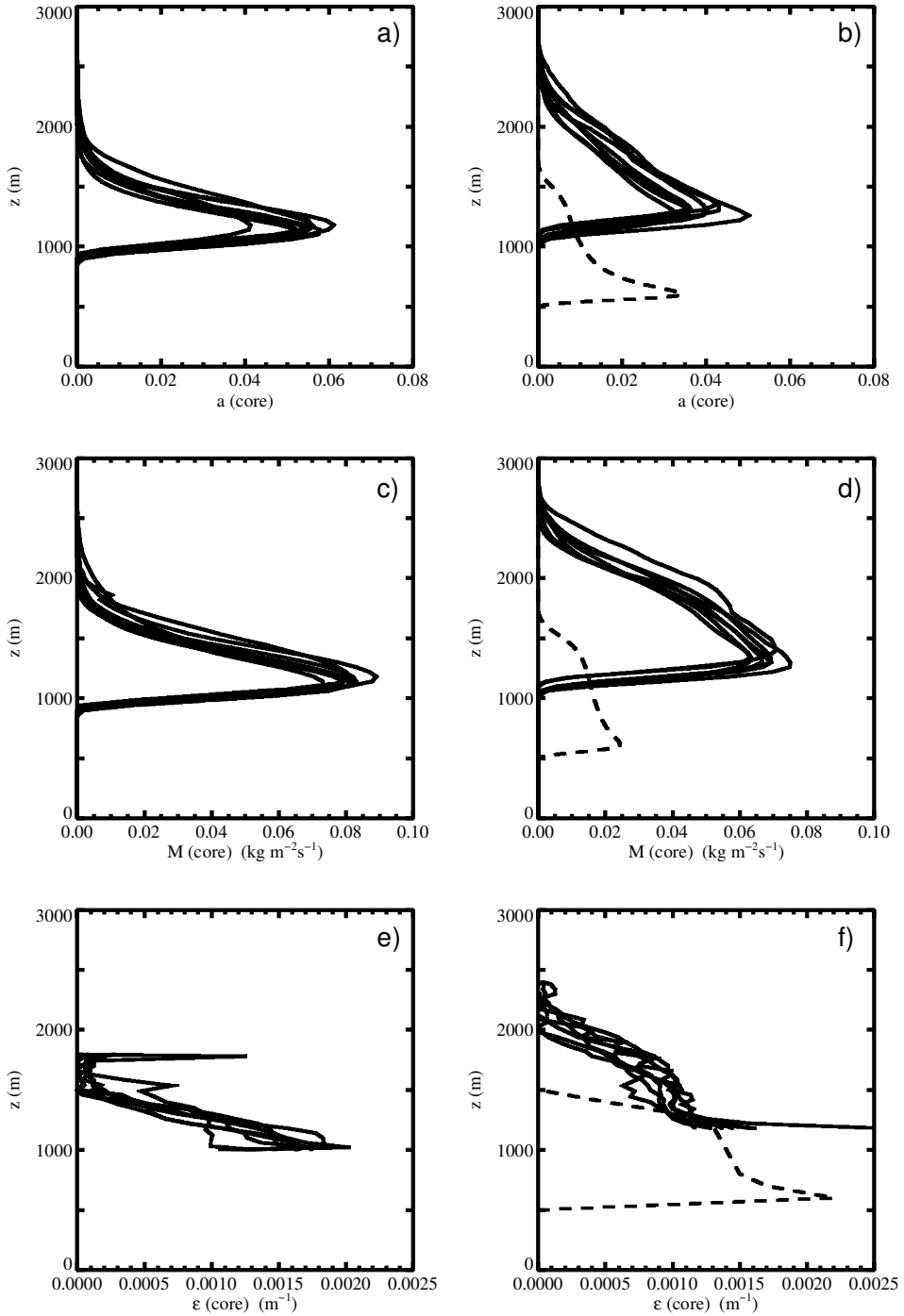


Figure 8. Profiles from the eight models at 1830 UTC (left column) and 2030 UTC (right column). (a)–(b) core fraction, (c)–(d) core mass flux and (e)–(f) core fractional entrainment rate. In the right column the dotted lines show the BOMEX results (simulation HR-CONV) from Brown (1999a).

from around $0.080 \text{ kg m}^{-2}\text{s}^{-1}$ at 1830 UTC to $0.055 \text{ kg m}^{-2}\text{s}^{-1}$ at 2130 UTC, while w_* is approximately constant over this period.

The fractional entrainment rates in the middle of the cloud layer of around 0.001 m^{-1} at 2030 UTC are approximately 35% smaller than those from BOMEX. However, this difference does appear to be largely explicable in terms of the previously developed scaling arguments of Grant and Brown (1999). They suggested that the fractional entrainment rate should scale as $(1/z_{\text{cld}})(w^*/m_b)$. Here z_{cld} is the depth of the cloud layer (estimated based on an undilute parcel ascent), $m_b = M_b/\rho$ where M_b is the maximum mass flux just above cloud base, and w^* is a cloud-layer velocity-scale (based on z_{cld} , m_b and the average buoyancy excess of an undilute parcel lifted through the cloud layer). The diagnosed values of $(1/z_{\text{cld}})(w^*/m_b)$ are approximately 45% smaller for the present case (at 2030 UTC) than for BOMEX (with most of the difference coming through the increase in m_b), and thus the difference in entrainment rates is largely explained. Again, the reasonable success of this scaling points to this case not being fundamentally different to those previously studied. However, it should be noted that the scaling performed poorly when used on datasets from up to 1830 UTC. This appeared to be primarily because a lack of instability in the mean profiles (see next section) led to the undilute parcel ascent significantly overestimating the cloud-layer depth. Use of the actual cloud depth (rather than that estimated through the undilute ascent) did improve the performance of the scaling at these times.

4. ADDITIONAL SENSITIVITY TESTS

A large number of sensitivity tests were performed by the various modelling groups in addition to the standard run. These fell into two categories—numerical tests, and tests examining the sensitivity to changing some aspect of the physical problem (e.g. changing the initial profiles or the surface fluxes). The results of some of the former will be briefly mentioned later, as showing a lack of sensitivity to some of the numerical choices made increases the level of confidence in the results. The range of the latter category is too broad to be able to include in this paper, although some tests assessing the sensitivity to changing the initial profiles have already been mentioned in connection with the modelled cloud base. Here we will concentrate on tests designed to investigate one specific question: Why did the cloud layer deepen so slowly in the standard run?

(a) *Numerical sensitivity tests*

On the numerical side, the robustness of the results obtained with eight different models already suggests that some of the numerical choices are not critical. This was further confirmed by performing tests with the Met Office model switching between monotone and centred advection, and also between an anelastic and Boussinesq formulation. The changes were generally small (although statistically significant in some cases, when judged against an ensemble of eight runs identical but for a change of initial random seed) and did not move the results outside the envelope of results provided by the eight standard simulations. Increasing the size of the horizontal domain (to $19.2 \times 19.2 \text{ km}$) with fixed grid spacing did not have a statistically significant impact, and neither did using a deeper domain. Even a factor of five reduction in horizontal grid spacing led to changes which were barely statistically significant (just a slight reduction in the maximum depth of penetration into the inversion, as found by Brown (1999a) for the BOMEX case), and which were again smaller than the spread of results from the eight standard runs. Hence, the results do appear to be numerically robust.

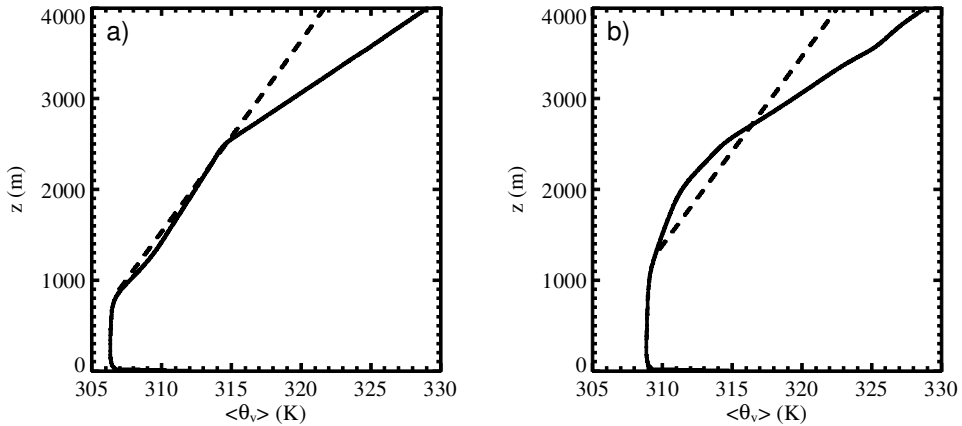


Figure 9. Mean virtual-potential-temperature profiles at (a) 1630 and (b) 2030 UTC (solid lines). The dashed lines show the virtual potential temperature of a parcel starting with the mean properties at cloud base and lifted without mixing through the domain.

(b) *Understanding the slow rate of growth of the cloud layer*

As shown in Fig. 5, the cloud layer in this case deepens only slowly, taking around six hours to reach its maximum depth. This behaviour was initially a surprise, and therefore some extra simulations were carried out with the Met Office model in order to understand what controls the rate of growth. It should be emphasized that these extra simulations were designed to be pure sensitivity tests and that they do not seek to match ARM observations.

One early suggestion was that the relatively dry atmosphere might be inhibiting cloud growth. However, tests with the initial $\langle r_T \rangle$ profile moistened above 1300 m (with the $\langle \theta \rangle$ profile modified slightly in order to keep the buoyancy profile unchanged) gave results almost identical to the standard run. The clue to the cause of the slow growth is in fact contained in Fig. 4, which shows that the modelled $\langle \theta \rangle$ profiles evolved in time in such a way as to become less stably stratified in the cloud layer. The effect is shown more clearly in Fig. 9 which shows the virtual-potential-temperature profiles θ_v at 1630 and 2030 UTC from the Met Office model simulation of the standard case. Also shown is the virtual potential temperature of an undilute parcel, starting with the mean properties at cloud base and lifted without mixing through the domain. At 1630 UTC it can be seen that this parcel does not become positively buoyant relative to the mean, as what will become the cloud layer has a profile which is close to conditionally neutral. Gradually the mean profile evolves to become more conditionally unstable, and by 1830 UTC (not shown) an undilute ascent from cloud base would be positively buoyant up to the inversion at 2500 m. However, real ascents are not undilute, and due to mixing with the environment the clouds at 1830 UTC still reach only around 2000 m. Only once the mean profile has become still more conditionally unstable—at around 2030 UTC—is it possible for the clouds to approach their maximum depth. Note that at this time, in the lower part of the cloud layer, $\partial \theta_v / \partial z$ of the undilute parcel exceeds that of the environment by around 2.5 K km^{-1} . This is almost exactly the same as the level of conditional instability of the quasi-steady BOMEX profile (Grant and Brown 1999). Hence it appears that the clouds grow slowly in the present case as the simulations cannot sustain full-depth clouds until the profiles have evolved in order to show instability comparable to that in the BOMEX case.

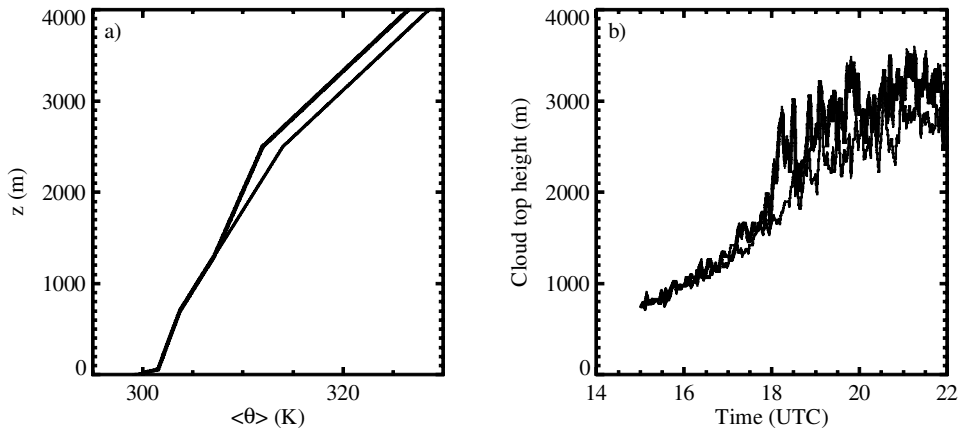


Figure 10. (a) Initial potential-temperature profiles from the standard run (light) and from the sensitivity test with a less stable profile (heavy). (b) Time series of cloud-top height from these two runs (unsmoothed).

In order to confirm the hypothesis that it is the lack of instability in the initial profiles that leads to the slow growth of the cloud layer in the standard case, a sensitivity test was performed with a modified initial potential-temperature profile as shown in Fig. 10(a). This profile is 1.7 K km^{-1} less stable than the standard profile between 1300 and 2500 m. The resulting time series of cloud-top height in this simulation is shown in Fig. 10(b). At first the evolution is almost identical to that of the standard run, as the profiles low down are unchanged. However, once the less stable layer is reached, the rise of cloud top is, as expected, much more rapid. The mass flux and fractional entrainment-rate profiles in this run (not shown) also achieve the shapes characteristic of a quasi-equilibrium cumulus layer an hour or so earlier than in the standard run.

5. CONCLUSIONS

This paper has described large-eddy simulations of the development of shallow cumulus over land. The case has been based on an idealization of ARM observations. The strong, time-varying forcing might have been expected to make this a more difficult case for the models than the previously studied cases of shallow cumulus over the sea. However, the results of eight independent models have proved to be encouragingly consistent. Further sensitivity studies looking at the effects of increasing resolution and domain size have also increased confidence in the robustness of the results.

The LES results for the subcloud layer have been shown to be consistent with well-established convective boundary-layer scalings. Direct validation of the cloud layer results is difficult (although the tendency of the models to have cloud cover decreasing with time is at least broadly consistent with the observations). In this region it has been found that many of the results previously found in over-sea cases are still applicable. For example, cloud cover and mass flux decrease with height. Changes in the magnitudes of the mass fluxes and fractional entrainment rate also appear to be largely explicable in terms of simple scalings.

One initially surprising aspect of the LES results for this case was the slow growth of the maximum depth of the cumulus clouds. It has been suggested that this was largely due to the initial profiles used, with a buoyancy structure which was more conditionally unstable being found to lead to a more rapid rise of cloud top.

A primary motivation for this work was to produce understanding and datasets which might help in the development and testing of parametrizations of shallow cumulus convection for use in large-scale numerical weather-prediction and climate models. Indeed, as reported by Lock *et al.* (2000), the LES results for this case have already been used in testing some aspects of the boundary-layer scheme used in the Met Office global models. In many ways the similarity of the cloud-layer structures in the BOMEX and ARM cases is encouraging in terms of the development of these schemes, as it suggests that there is no fundamental reason why a parametrization which performs well for one case should not also do so for the other. However, the preliminary results of an intercomparison of the performance of single-column models for the present ARM case (Geert Lenderink, personal communication) show a wide scatter. This suggests that there is still much work to be done in terms of understanding the performance of the single-column models, and in developing and refining the parametrizations that they use. Detailed comparisons with the LES results will be crucial in this exercise.

ACKNOWLEDGEMENTS

Data were obtained from the ARM Program, sponsored by the US Department of Energy, with the help of Jon Gottschalk. The authors also wish to acknowledge the contributions to this work of the participants at the intercomparison workshop which was held at the National Center for Atmospheric Research in January 2000.

APPENDIX

This appendix contains the remaining detailed specification of the case required in order for any reader to repeat it using either a large-eddy or single-column model.

The initial profiles of $\langle\theta\rangle$ and $\langle r_T\rangle$ were shown in Fig. 1, and time series of the imposed surface fluxes in Fig. 2. However, to avoid having to attempt to read values off the plots, the specification is given in Tables A.1 and A.2. Linear interpolation was used to obtain values between the specified heights and times.

As noted in the main text, the effects of representation of large-scale advection and radiation were small compared with that of the surface forcing. The large-scale forcing terms were a simple representation of the profiles estimated using a variational method based on observations from over the entire SGP site (Zhang and Lin 1997; Zhang *et al.* 2001). The radiative forcing was estimated by diagnosing the net heating

TABLE A.1. INITIAL PROFILES OF $\langle\theta\rangle$ AND $\langle r_T\rangle$ (SEE TEXT)

z (m)	$\langle\theta\rangle$ (K)	$\langle r_T\rangle$ (g kg ⁻¹)
0.0	299.00	15.20
50.0	301.50	15.17
350.0	302.50	14.98
650.0	303.53	14.80
700.0	303.70	14.70
1300.0	307.13	13.50
2500.0	314.00	3.00
5500.0	343.20	3.00

Linear interpolation was used to obtain values at intermediate heights.

TABLE A.2. IMPOSED SURFACE SENSIBLE-HEAT (H) AND LATENT-HEAT (LE) FLUXES

Time (UTC)	H (W m ⁻²)	LE (W m ⁻²)
1130	-30	5
1530	90	250
1800	140	450
1900	140	500
2130	100	420
0000	-10	180
0200	-10	0

Linear interpolation was used to obtain the fluxes between the specified times.

TABLE A.3. MAGNITUDES OF LARGE-SCALE ADVECTIVE FORCING AND RADIATIVE TENDENCIES TO BE APPLIED IN LOWEST 1000 M

Time (UTC)	A_θ (K h ⁻¹)	R_θ (K h ⁻¹)	A_{r_T} (g kg ⁻¹ h ⁻¹)
1130	0.000	-0.125	+0.080
1430	0.000	0.000	+0.020
1730	0.000	0.000	-0.040
2030	-0.080	0.000	-0.100
2330	-0.160	0.000	-0.160
0200	-0.160	-0.100	-0.300

Reduced tendencies were applied above 1000 m, as described in the text. Linear interpolation was used to calculate forcings at intermediate times.

rates from a simulation with the Met Office model using an interactive two-stream radiation code (Edwards and Slingo 1996). Separate tests confirmed that applying a simple representation of the averaged heating profiles gave results very similar to those obtained using the interactive scheme. This is consistent with the experience of Cuijpers (1994) and Jiang and Cotton (2000) for low-cloud-cover shallow-cumulus simulations.

Table A.3 gives the values of A_θ , R_θ and A_{r_T} which were used to scale the values of the large-scale advective tendency of θ , the radiative tendency to be applied to θ , and the large-scale advective tendency of r_T , respectively. The values are given at various times, and linear interpolation was used to obtain values at intermediate times. Below 1000 m a forcing term of $A_\theta + R_\theta$ was applied to the θ equation and of A_{r_T} to the r_T equation. The size of these terms was decreased linearly to zero between 1000 m and 2000 m, and no forcing was applied for $z > 2000$ m.

REFERENCES

Brown, A. R.	1999a	The sensitivity of large-eddy simulations of shallow cumulus convection to resolution and subgrid model. <i>Q. J. R. Meteorol. Soc.</i> , 125 , 469–482
	1999b	Large-eddy simulation and parametrization of the effects of shear on shallow cumulus convection. <i>Boundary-Layer Meteorol.</i> , 91 , 65–80
Browning, K. A.	1993	The GEWEX Cloud System Study (GCSS). <i>Bull. Am. Meteorol. Soc.</i> , 74 , 387–399
Cuijpers, J. W. M.	1994	‘Large eddy simulation of cumulus convection’. PhD thesis, Delft University of Technology

- Edwards, J. M. and Slingo, A. 1996 Studies with a flexible new radiation code I: Choosing a configuration for a large-scale model. *Q. J. R. Meteorol. Soc.*, **122**, 689–719
- Grant, A. L. M. 1986 Observations of boundary-layer structure made during the KONTUR experiment. *Q. J. R. Meteorol. Soc.*, **112**, 825–841
- Grant, A. L. M. 2001 Cloud-base fluxes in the cumulus-capped boundary layer. *Q. J. R. Meteorol. Soc.*, **127**, 407–421
- Grant, A. L. M. and Brown, A. R. 1999 A similarity hypothesis for shallow cumulus transports. *Q. J. R. Meteorol. Soc.*, **125**, 1913–1936
- Jiang, H. and Cotton, W. R. 2000 Large eddy simulation of shallow cumulus convection during BOMEX: Sensitivity to microphysics and radiation. *J. Atmos. Sci.*, **57**, 582–594
- Lenschow, D. H., Wyngaard, J. C. and Pennel, W. T. 1980 Mean-field and second moment budgets in a baroclinic, convective boundary layer. *J. Atmos. Sci.*, **37**, 1313–1326
- Lock, A. P., Brown, A. R., Bush, M. R., Martin, G. M. and Smith, R. N. B. 2000 A new boundary layer scheme for the Unified Model. Part I: Scheme description and single-column model tests. *Mon. Weather Rev.*, **128**, 3187–3199
- Mason, P. J. 1992 Large-eddy simulation of dispersion in convective boundary layers with wind shear. *Atmos. Env.*, **26A**, 1561–1571
- Moeng, C.-H. and Sullivan, P. P. 1994 A comparison of shear and buoyancy driven planetary boundary layer flows. *J. Atmos. Sci.*, **51**, 999–1022
- Nicholls, S. and LeMone, M. A. 1980 The fair weather boundary layer in GATE: The relationship of subcloud fluxes and structure to the distribution and enhancement of cumulus clouds. *J. Atmos. Sci.*, **37**, 2051–2067
- Nicholls, S. and Readings, C. J. 1979 Aircraft observations of the lower boundary layer over the sea. *Q. J. R. Meteorol. Soc.*, **105**, 785–802
- Nieuwstadt, F. T. M., Mason, P. J., Moeng, C.-H. and Schumann, U. 1991 Large-eddy simulation of the convective boundary layer: A comparison of four computer codes. Pp. 343–367 in *Turbulent Shear Flows 8*, Eds. F. Durst *et al.* Springer Verlag, Berlin
- Siebesma, A. P. and Cuijpers, J. W. M. 1995 Evaluation of parametric assumptions for shallow cumulus convection. *J. Atmos. Sci.*, **52**, 650–666
- Siebesma, A. P. and Holtslag, A. A. M. 1996 Model impacts of entrainment and detrainment rates in shallow cumulus convection. *J. Atmos. Sci.*, **53**, 2354–2364
- Stevens, B., Ackerman, A. S., Albrecht, B. C., Brown, A. R., Chlond, A., Cuxart, J., Duynkerke, P. G., Lewellen, D. C., MacVean, M. K., Sanchez, E., Siebesma, A. P. and Stevens, D. E. 2001 Simulations of trade-wind cumuli under a strong inversion. *J. Atmos. Sci.*, **58**, 1870–1891
- Tiedtke, M., Heckley, W. A. and Slingo, J. 1988 Tropical forecasting at ECMWF: The influence of physical parametrization on the mean structure of forecasts and analyses. *Q. J. R. Meteorol. Soc.*, **114**, 639–664
- Zhang, M. H. and Lin, J. L. 1997 Constrained variational analysis of sounding data based on column-integrated budgets of mass, heat, moisture and momentum: Approach and application to ARM measurements. *J. Atmos. Sci.*, **54**, 1503–1524
- Zhang, M. H., Lin, J. L., Cederwall, R. T., Yio, J. J. and Xie, S. C. 2001 Objective analysis of the ARM IOP data: Method and sensitivity. *Mon. Weather Rev.*, **129**, 295–311